Collision excitation of sodium cyanide molecule by helium at low temperature

C. Gharbi,[1] Y. Ajili,[2] D. Ben Abdallah,[1,2] M. Mogren Al Mogren[3] and M. Hochlaf[4]⋆

[1]*Laboratoire de Spectroscopie et Dynamique Moléculaire, Université de Tunis, Ecole Nationale Supérieure d'Ingénieurs de Tunis, 5 Av Taha Hussein,1008 Tunis, Tunisia*
[2]*Laboratoire de Spectroscopie Atomique, Moléculaire et Applications – LSAMA, Université de Tunis-El Manar, Tunis, Tunisia*
[3]*Chemistry Department, Faculty of Science, King Saud University, PO Box 2455, Riyadh 11451, Kingdom of Saudi Arabia*
[4]*Laboratoire Modélisation et Simulation Multi Echelle, Université Paris-Est, MSME UMR 8208 CNRS, France*

ABSTRACT

Cyanides/isocyanides are the most common metal-containing molecules in interstellar medium. In this work, quantum scattering calculations were carried out to determine the rotational (de-)excitation of the most stable form of the sodium cyanide molecule, t-NaCN, in collision with the helium atom. Rate coefficients for the first 43 rotational levels (up to $j_{K_a K_c} = 6_{3,3}$) of NaCN were determined for kinetic temperatures ranging from 1 to 30 K. Prior to that, we constructed a new three-dimensional potential energy surface (3D-PES) for the t-NaCN–He interacting system. These electronic structure computations are done at the CCSD(T)-F12/aug-cc-pVTZ level of theory. Computations show the dominance of $\Delta j = \Delta K_c = -1$ transitions, which is related to the dissymmetric shape of the t-NaCN–He 3D-PES. The NaCN–He rate coefficients are of the same order of magnitude ($\sim 10^{-11}$ cm) as those of other metal CN-containing molecules such as MgCN and AlCN in collision with He. This work is a contribution for understanding and modelling the abundances and chemistry of nitriles in astrophysical media.

Key words: ISM: abundances.

1 INTRODUCTION

The number of metal-bearing molecules detected in space has never stopped growing (Ziurys et al. 2002; McGuire 2018). Their stabilities, abundances, as well as their synthesis are still of concern to many communities working on experimental and theoretical astrochemistry. Structural, spectroscopic, and collisional data are useful for modelling their abundances in astrophysical media (He et al. 2008; Halfen & Ziurys 2011; Müller, Halfen & Ziurys 2012; Senent, Dumouchel & Lique 2012). Since the identification of the first metal halide in the envelope of the C-rich star IRC+10216 (Cernicharo & Guelin 1987), a large series of metal cyanide/isocyanide compounds containing Na, Mg, Al, Si, K, Fe have been discovered (Kawaguchi et al. 1993; Turner, Steimle & Meerts 1994; Guélin et al. 2000; Ziurys et al. 2002; Guélin et al. 2004; Pulliam et al. 2010; Zack, Halfen & Ziurys 2011). The main part of cyanides observations has been performed in IRC+10216 envelope and other circumstellar sources such as CRL 2688 (Highberger et al. 2001) and VRL618 (Ziurys et al. 1995; Highberger & Ziurys 2003; Pulliam et al. 2010).

The theoretical calculations showed that the most stable form of NaCN has a T-shaped structure, namely t-NaCN (Senent et al.

2012). t-NaCN was first discovered confined in the IRC+10216 inner shell (Turner et al. 1994) via its 2 and 3 mm rotational transitions in the $K_a = 0$ asymmetry component. It is a remarkably abundant circumstellar molecule (Halfen & Ziurys 2011). More recent sensitive spectral survey (~ 1 mm) of IRC+10216 (Tenenbaum et al. 2010) showed that this molecule exhibited the fourth highest number of spectral lines, with asymmetry components present as high as $K_a = 7$. On the experimental side, Ziurys and co-workers (Halfen & Ziurys 2011; Müller et al. 2012) have conducted new measurements on the millimeter/submillimeter spectrum of this molecule up to 570 GHz. Multiple K_a asymmetry components were recorded in each rotational transition up to $K_a = 5$ or 6. In light of their laboratory results and the latest spectral survey, Halfen & Ziurys (Halfen & Ziurys 2011) revised the fractional abundance of this floppy molecule in IRC+10216 to be f(NaCN/H$_2$) $\sim 1 \times 10^{-8}$, comparable to that of c-C$_3$H$_2$. Note that in addition to t-NaCN, two linear isomers (l-NaNC and l-NaCN) are predicted by computations. Both l-NaNC and l-NaCN are not detected yet. They are located at higher energies with respect to t-NaCN. Relatively large potential barriers prohibit interconversion between these isomers at low temperatures. Anyway, in interstellar medium (ISM) and stellar envelopes where temperatures are relatively low, isomers are supposed to behave as different species.

The molecular abundances in the ISM depend on molecular stabilities, reaction probabilities, and radiative and collisional ex-
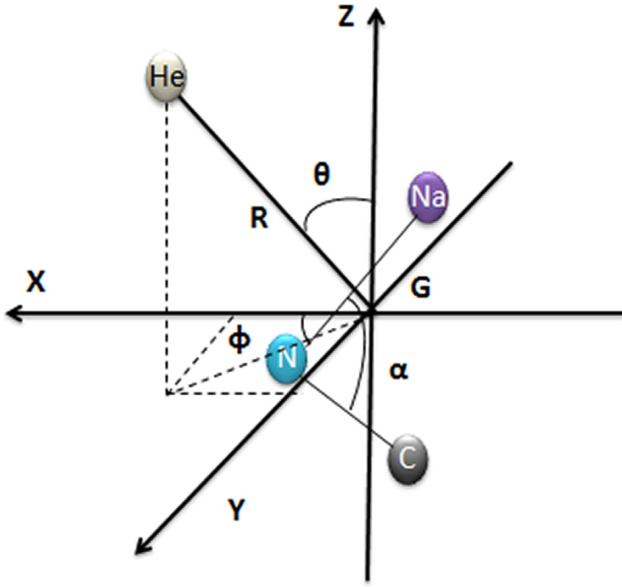
Figure 1. Definition of the Jacobi coordinates (R, θ, Φ) of NaCN–He complex used in this work. G corresponds to the centre of mass of NaCN.

citations. Since collisions and radiative processes participate into altering the populations of the molecular rotation-vibration states, astrophysicists need collision rate coefficients of molecules with the most abundant gases in the universe i.e. H, H_2, and He. In this work, we mainly focus on the calculations of rate coefficients of rotational (de-)excitation of *t*-NaCN colliding with He at low temperatures. Helium atom is often assumed to be a model for para-H_2 ($j = 0$) (Lique et al. 2008). Using He as a substitute of H_2 is an approximation to estimate the collision rate coefficients with reduced computational cost. Such approximation most of the time does not work. The He rate coefficients can differ by a factor of 3 from those of H_2 depending on the transition and the temperature (Lique et al. 2009; Najar et al. 2009).

First, we generated a three-dimensional potential energy surface (3D-PES) for the *t*-NaCN–He weakly bound interacting system. This 3D-PES is mapped in intermonomer Jacobi coordinates (Fig. 1) using the explicitly correlated coupled cluster (CCSD(T)-F12) approach. Secondly, we derived an analytical expansion of this 3D-PES. Thirdly, we carried out quantum dynamical computations on this newly developed 3D-PES. Thus, we deduced the cross-sections and collision rates for the rotational (de-)excitation of *t*-NaCN colliding with He at temperatures between 1 and 30 K. The present collisional rate coefficients may be used for determining the abundance of *t*-NaCN in cold astrophysical media. Indeed, Quintana-Lacaci et al. (2017) recently pointed out the need of such data for modelling and understanding sodium cyanide chemistry there.

2 GENERATION OF THE 3D-PES OF NACN–HE INTERACTING SYSTEM

2.1 Electronic structure computations

All *ab initio* electronic computations were done using the MOLPRO 2015 package (Werner et al. 2015). Here, we focused on the study of the T-shaped form of sodium cyanide, *t*-NaCN, in collision with the spherical structureless target He atom at low temperatures. *t*-NaCN (denoted hereafter as NaCN) is an asymmetric-top molecule. For

energies below its first vibrational state [i.e. < 173 cm^{-1} (Müller et al. 2012; Senent et al. 2012)], NaCN can be considered as a rigid bent rotor. We made multiconfigurational calculations using the complete active space self-consistent field (CASSCF) method (Knowles & Werner 1985; Werner & Knowles 1985) in order to inspect the electronic wavefunction of the NaCN–He van der Waals complex. These test computations showed that the weight of the dominant configuration in this wavefunction is greater than 0.93 for all investigated geometries. This validated hence the use of monoconfigurational approaches for mapping the potential energy surface of this colliding system.

The ground electronic state of the weakly bound NaCN (X^1A')–He (^1S) system is a singlet with C_1 space symmetry. The NaCN–He 3D-PES is mapped using the explicitly correlated coupled cluster method with single, double, and triple perturbative excitations CCSD(T)-F12 (Adler, Knizia & Werner 2007; Knizia, Adler & Werner 2009) in conjunction with the augmented correlation consistent-polarized valence triple zeta (aug-cc-pVTZ) basis set (Dunning 1989; Kendall, Dunning & Harrison 1992). We also used the MOLPRO default choices for the density fitting and resolution of identity basis sets (Yousaf & Peterson 2008). The validity of the present methodology for the generation of multidimensional potential energy surfaces of weakly bound molecular systems was discussed in many previous works either in the regions of the potential wells and at long-range separations. For illustration, we give in Fig. S1 of the Supplementary Material, the one-dimensional cuts of the NaCN–He 3D-PES along the R coordinate as obtained at the CCSD(T)-F12/aug-cc-pVTZ level and their comparison to analytical potential using multipolar expansions. This figure shows good agreement between both sets of data (see Supplementary Material for more details). It turns out that the CCSD(T)-F12/aug-cc-pVTZ PESs are as accurate as those obtained using the standard coupled cluster approach extrapolated to complete basis set limit (CCSD(T)/CBS), while a strong reduction of the computational costs (both CPU and disc occupancy) is achieved (Lique, Kłos & Hochlaf 2010; Ajili et al. 2013; Al Mogren et al. 2014; Hochlaf 2017).

The 3D-PES of NaCN–He is mapped in the Jacobi coordinates (R, θ, Φ) as shown in Fig. 1. The (GX), (GY), and (GZ) axes are placed along the three principal axes of inertia of the NaCN molecule. R is the distance from the centre of mass G of NaCN molecule to the He atom. θ corresponds to the angle between $\mathbf{R}$ and the (GZ) axis. Φ is the angle between the molecular plane and $\mathbf{R}$. The intermolecular coordinates of the NaCN asymmetric molecule were frozen at their equilibrium values: $r_{NaN} = 4.264$ bohr, $r_{CN} = 2.230$ bohr and the in-plane bending NaCN angle was set at $67.82°$ (Senent et al. 2012).

The electronic *ab initio* calculations of the NaCN–He 3D-PES system were carried out for θ and Φ angles ranging from $0°$ to $180°$ with an uniform step of $10°$ and $15°$, respectively. For each set of θ and Φ, 40 values of the intermolecular distance R were chosen, i.e. $R = [3.5, 3.75, 4.0, 4.25, 4.5, 4.75, 5.0, 5.25, 5.5, 5.75, 6.0, 6.25, 6.5, 6.75, 7.0, 7.25, 7.5, 7.75, 8.0, 8.25, 8.5, 8.75, 9.0, 9.25, 9.5, 9.75, 10.0, 10.5, 11.0, 12.0, 13.0, 14.0, 16.0, 18.0, 20.0, 25.0, 30.0, 40.0, 50.0, 100.0]$ bohr. This grid resulted into 760 non-equivalent geometries treated in the C_1 point group symmetry. It's worth mentioning that in the interaction potential $V(R, \theta, \Phi)$ calculations, the basis set superposition error (BSSE) was corrected at all geometries using the Boys and Bernardi (Boys & Bernardi 1970) counterpoise procedure:

$$V(R, \theta, \Phi) = E_{NaCN-He}(R, \theta, \Phi) - E_{NaCN}(R, \theta, \Phi)$$
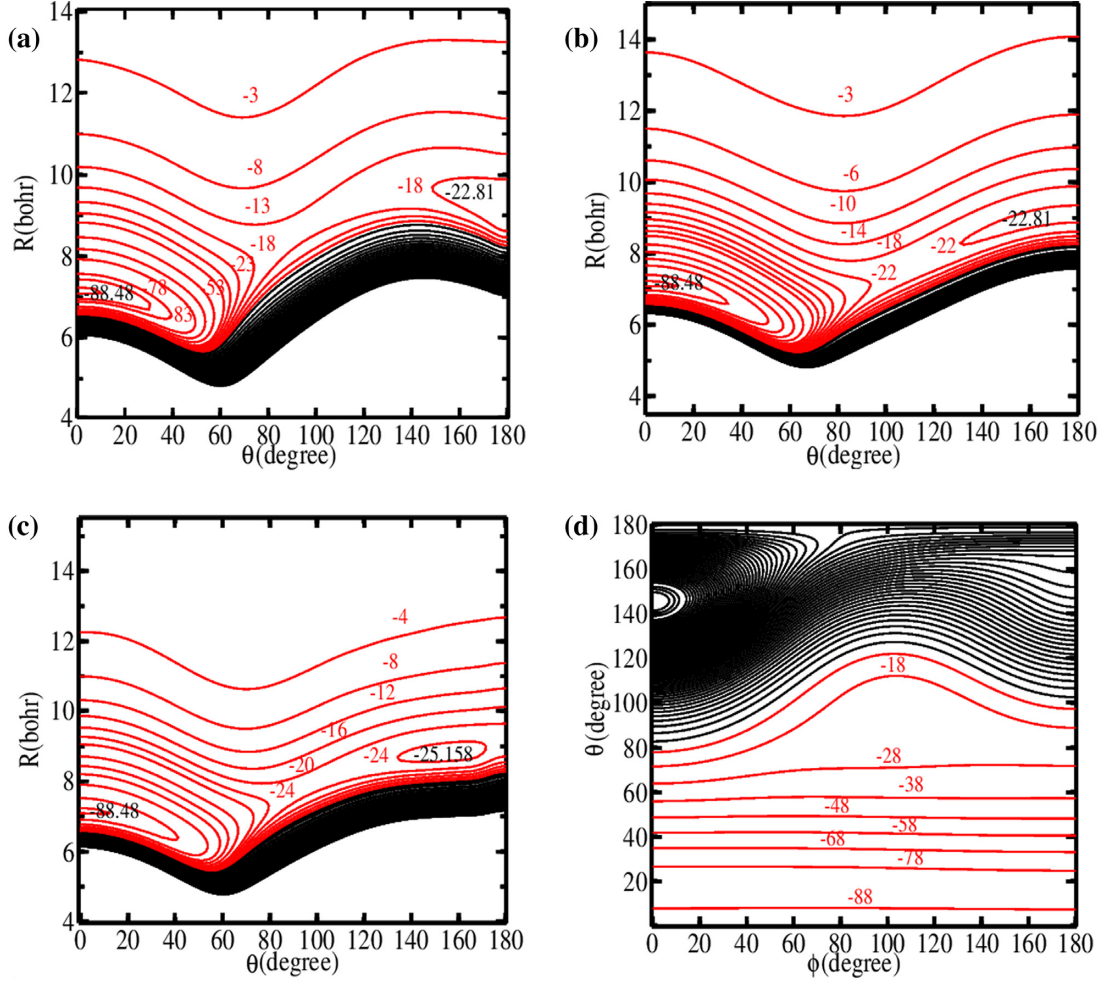$$- E_{He}(R, \theta, \Phi), \qquad (1)$$

Figure 2. 2D contour plots of the 3D-PES of the NaCN–He interacting system along the R and θ coordinates for fixed Φ values. In (a), $\Phi = 0°$. In (b), $\Phi = 90°$. In (c), $\Phi = 180°$. In (d), we give the cuts along the angular coordinates θ and Φ for $R = 7.2$ bohr. Energies are in cm^{-1}. Black contour lines represent repulsive interaction energies. The reference energy is the energy of the separated NaCN and He species.

where $E_{\text{NaCN–He}}(R, \theta, \Phi)$ is the total electronic energy of the NaCN–He complex. $E_{\text{NaCN}}(R, \theta, \Phi)$ and $E_{\text{He}}(R, \theta, \Phi)$ are the total energies of NaCN and of He, respectively. All these energies are evaluated in the full basis set of the complex. Moreover, we corrected for the non-size consistency of the CCSD(T)-F12 method. Thus the 3D-PES was shifted up by subtracting the value of the interaction energy at $R = 100$ bohr (of ~ -1.9 cm^{-1}).

Fig. 2 displays the 2D cuts of the 3D-PES of the NaCN–He system along the two Jacobi coordinates R and θ for $\Phi = 0°$, $90°$, and $180°$. One can see that the potential has the same shape for $\Phi = 0°$ and $\Phi = 180°$, whereas a different behaviour along R and θ is observed for $\Phi = 0°$ and for $\Phi = 90°$ (see below). Fig. 2(d) depicts the 2D cut of the NaCN–He PES along the angular coordinates θ and Φ for $R = 7.2$ bohr. Practically, there is no dependence on Φ for $\theta \leq 60°$. This figure shows that the interaction potential between NaCN and He is strongly anisotropic, particularly along the R and θ coordinates. This anisotropy will play a great role in the rotational energy transfer to the cyanide sodium molecule during the collision.

Table 1 lists the geometries of the stationary points of the NaCN–He PES and their corresponding potential energies for $\Phi = 0°$, $\Phi = 90°$, and $\Phi = 180°$. The global minimum of this 3D-PES is located at $R = 7.20$ bohr, $\theta = 0°$, and $\Phi = 0°$ coordinates. At

this geometry, the well depth is 88.49 cm^{-1} (Table 1). In addition, we can see a second minimum for $R = 9.10$ bohr and $\theta = 180°$ with a well depth of 22.81 cm^{-1}. Both structures are separated by a transition state with $R = 9.30$ bohr, $\theta = 105°$, and $V = -14.00$ cm^{-1}. For $\Phi = 90°$, the PES presents two minima located at $R = 7.20$ bohr and $\theta = 0°$ and $R = 9.10$ bohr and $\theta = 180°$ separated by a transition state at $R = 7.60$ bohr and $\theta = 107°$ and $V = -21.01$ cm^{-1}. The potential well at this geometry is $V = 88.49$ cm^{-1}. For $\Phi = 180°$, we compute two minima separated by a transition state. The first minimum can be found at $R = 7.2$ bohr and $\theta = 0°$ with a well depth of 88.49 cm^{-1}. The second minimum is located at $R = 8.80$ bohr and $\theta = 155°$ with $V = -25.16$ cm^{-1}. The transition state is for $R = 7.90$ bohr, $\theta = 103°$, and $V = -21.00$ cm^{-1}. In sum, all identified minima and transition states are located below the dissociation energy of the NaCN–He complex. For other weakly bound molecular systems, we established that this special PES shape is associated with complex quantum effects, including quantum tunnelling, vibrational memory, and quantum localization effects (Ajili et al. 2016; Lara-Moreno et al. 2019). Therefore, our work suggests that both the theoretical and experimental rovibrational spectroscopy of the NaCN–He van der Waals system cannot be understood without considering these effects.

Table 1. Characteristics of some stationary points of the 3D-PES of NaCN–He complex. Distances (R) are in bohr and angles in degrees. V (in cm^{-1}) is the dissociation energy.

		$\phi = 0°$			
$\theta = 0°$		$\theta = 105°$		$\theta = 180°$	
R	V	R	V	R	V
7.20	−88.49	9.30	−14.00	9.10	−22.81
		$\phi = 90°$			
$\theta = 0°$		$\theta = 107°$		$\theta = 180°$	
R	V	R	V	R	V
7.20	−88.49	7.60	−21.01	9.10	−22.81
		$\phi = 180°$			
$\theta = 0°$		$\theta = 103°$		$\theta = 155°$	
R	V	R	V	R	V
7.20	−88.49	7.90	−21.00	8.80	−25.16

2.2 Analytic form of the 3D-PES

To perform the dynamical calculations, the 3D-PES was fitted to an analytical representation in terms of spherical harmonic expansion:

$$V(R, \theta, \Phi)$$
$$= \sum_{l=0}^{l_{max}} \sum_{m=0}^{m_{max}} v_{lm}(R) \frac{Y_{l,m}(\theta, \Phi) + (-1)^m Y_{l,-m}(\theta, \Phi)}{1 + \delta_{m0}}, \quad (2)$$

where $Y_{l,m}(\theta, \Phi)$ are the normalized spherical harmonics. $v_{lm}(R)$ are the radial functions to be optimized, and $\delta_{m,0}$ is the Kronecker delta.

From the PES grid including (19×13) values of (θ, Φ), we calculated $v_{lm}(R)$ coefficients for each R value of the radial grid by the least-square procedure. We took a full set of m values ($0 \leq m \leq l$) for l ranging from 0 to 11, whereas we considered $m_{max} = 6$ for $l_{max} = 12$. In total, we obtained 85 angular coefficients of $v_{lm}(R)$. The error percentage of these coefficients is less than 0.5 per cent for the long range ($R > 6$ bohr i.e. attractive part) and smaller than 5 per cent for the short range ($R < 6$ bohr i.e. repulsive part). The 3D-PES can be sent upon request.

3 DYNAMICAL CALCULATIONS

3.1 Rotational structure of NaCN

The rotational Hamiltonian of the NaCN asymmetric top molecule is given by the following expression:

$$H_{rot} = A j_x^2 + B j_y^2 + C j_z^2 - D_J j^4 - D_{JK} j^2 j_z^2 - D_K j_z^4, \quad (3)$$

where, A, B, and C are the rotational constants of NaCN. D_J, D_{JK}, and D_K are the first-order centrifugal distortion corrections. j_x^2, j_y^2, and j_z^2 are the square of the projections of the total angular momentum along the different principal molecular axes such that, $j^2 = j_x^2 + j_y^2 + j_z^2$.

For an asymmetric top molecule like NaCN, the rotational levels are conventionally labelled by j_{K_a, K_c}, where K_a and K_c are the projections of the total rotational angular momentum along the axis of symmetry for the prolate and oblate symmetric top limits. The energy diagram of NaCN rotational levels shown in Fig. 3 is constructed using the rotational and distortional constants as determined by Halfen & Ziurys (Halfen & Ziurys 2011) i.e. $A = 0.270\,33\,cm^{-1}$, $B = 0.2375\,cm^{-1}$, $C = 1.905\,94\,cm^{-1}$, $D_J = 5.003 \times 10^{-7}\,cm^{-1}$, $D_K = 2.59 \times 10^{-5}\,cm^{-1}$, and $D_{JK} = 1.1 \times 10^{-6}\,cm^{-1}$. Since NaCN is composed by three heavy atoms, the rotational structure is very complex with a high density of rotational levels with relatively small energy spacing between them (Fig. 3).
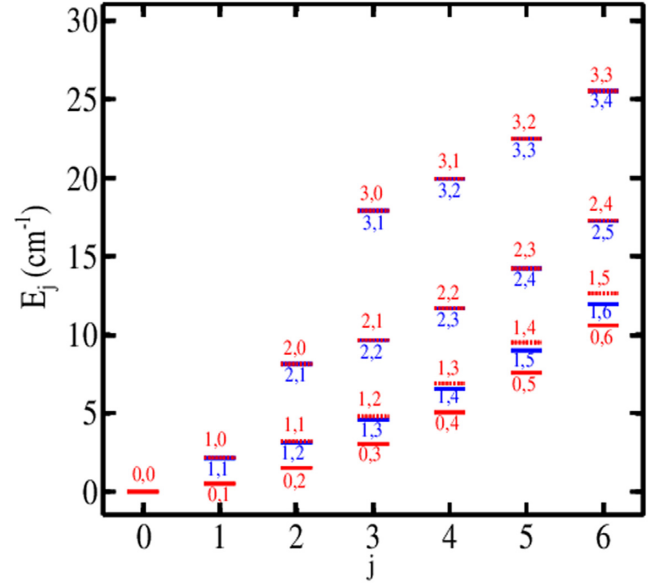

Figure 3. NaCN rotational energy levels for $j_{K_a K_c}$ up to $= 6_{3,3}$. These levels are labelled by the values of the rotational quantum number j (given along the abscissa) and the projection quantum numbers K_a and K_c.

Table 2 lists the frequencies of some dipole-allowed transitions detected in IRC+10216 (Turner et al. 1994) and CRL2688 regions (Highberger et al. 2001). They are also compared with those deduced using the spectroscopic parameters of Halfen & Ziurys (Halfen & Ziurys 2011). A close agreement between the two sets of data is observed.

3.2 Cross-sections

For scattering calculations, the fitted 3D-PES of the colliding system NaCN–He was incorporated in the MOLSCAT program (Hutson & Green 1994). The exact close-coupling (CC) method described in Refs. Garrison & Lester Jr. (1976), Green (1976), and Green (1979) was selected to determine the inelastic rotational cross-sections of the cyanide sodium molecule in collision with helium. We are only interested in transitions between the first 43 rotational levels. This corresponds to a maximum of rotational energy, $E_{rot} = 25.515\,cm^{-1}$, i.e. up to $j_{K_a, K_c} = 6_{3,3}$ level. The computation is done for total energies (rotational + kinetic) smaller than 170 cm^{-1}, i.e. below the threshold for the excitation of the bending vibrational mode

Table 2. Frequencies (in MHz) for selected dipole-allowed transitions of NaCN molecule as observed in IRC+10216 and in CRL2688. We give also those derived using rotational and distortional constants of Halfen & Ziurys (Halfen & Ziurys 2011). See text for more details.

$j_{K_a,K_c}-j'_{K_{a'},K_{c'}}$ transitions	Calculated[a]	Observed
$5_{0,5}-4_{0,4}$	75 749.3	77 836.7[b]
$6_{0,6}-5_{0,5}$	90 728.7	93 206.1[b]
$7_{0,7}-6_{0,6}$	105 618.3	108 472.0[b]
$9_{0,9}-8_{0,8}$	135 088.8	138 652.1[b]
$9_{0,9}-8_{0,8}$	135 088.8	138 651.9[c]
$10_{0,10}-9_{0,9}$	149 659.3	153 557.7[c]
$10_{3,8}-9_{3,7}$	152 216.1	156 541.2[c]
$10_{3,7}-9_{3,6}$	152 331.5	156 684.0[c]
$10_{2,8}-9_{2,7}$	154 020.1	158 616.4[c]
$6_{1,6}-5_{1,5}$	88 112.2	90 394.38[d]
$6_{0,6}-5_{0,5}$	90 728.7	93 206.09[d]
$6_{2,4}-5_{2,3}$	91 690.0	94 334.80[d]
$6_{1,5}-5_{1,4}$	94 148.4	96 959.81[d]
$9_{1,8}-8_{1,7}$	136 537.1	145 075.57[d]
$10_{2,8}-9_{2,7}$	152 216.1	158 616.77[d]

[a]This work.
[b]Turner et al. (1994).
[c]Highberger et al. (2001).
[d]Quintana-Lacaci et al. (2017).

of NaCN. The hybrid log-derivative propagator of Manolopoulos (Manolopoulos 1986) was used to determinate the solution of the coupled equations.

First, we tested the parameters of the integrator, which were adjusted to ensure convergence of the cross-sections over the whole energy range. For the total energy range ($1 \leq E \leq 170$ cm^{-1}), benchmarks showed that the rotational basis set associated with $j_{\max} = 12$ is sufficient to ensure the convergence of NaCN–He inelastic cross-sections for all transitions up to $j_{K_aK_c} = 6_{3,3}$. Since the size of the coupled equations and the necessary computer time for their resolution increase rapidly with the size of the basis set, the cut-off parameter $E_{\max} = 55$ cm^{-1} was used to remove some highly excited states that formally become open but in practice remain very weakly populated by transitions from the lowest levels. The integral cross-sections are obtained by summing the partial cross-sections over a sufficiently large number of values of the total angular momentum J_{tot} until convergence is reached. For example, for the total energy, $E = 170$ cm^{-1}, $J_{\text{tot}} = 35$ ensures a convergence to within 2 per cent for all considered inelastic transitions.

For the proper description of the resonances during the calculations and of the small energy spacing between the rotational levels, a fine energy grid was carefully chosen. We used a step of 0.1 cm^{-1} for 1 cm^{-1} < E < 50 cm^{-1}, of 0.2 cm^{-1} for 50 cm^{-1} < E < 100 cm^{-1}, and of 1 cm^{-1} for 100 cm^{-1} < E < 170 cm^{-1}.

Figs 4(a) and (b) present respectively the downward cross-sections for the transitions from the $5_{0,5}$ state to the $j_{K_{a'},K_{c'}}$ levels where $\Delta K_a = 0$ and $\Delta K_c = \Delta j (= -1, -2, -3, -4, -5)$ and those for some transitions where $\Delta K_a = 0$ and $\Delta K_c = \Delta j = -1$. The transitions associated with $\Delta j = -1$ are dominant. The rotational de-excitation cross-sections as well as the number and the height of the resonances decrease with increasing $|\Delta j|$. Resonances do not exist for cross-sections involving levels with large Δj due to the large threshold energy value. For fixed $\Delta j (= -1)$, cross-sections increase with increasing j. We can clearly notice that the detected transitions $5_{0,5}-4_{0,4}$ and $6_{0,6}-5_{0,5}$ are the dominant ones.
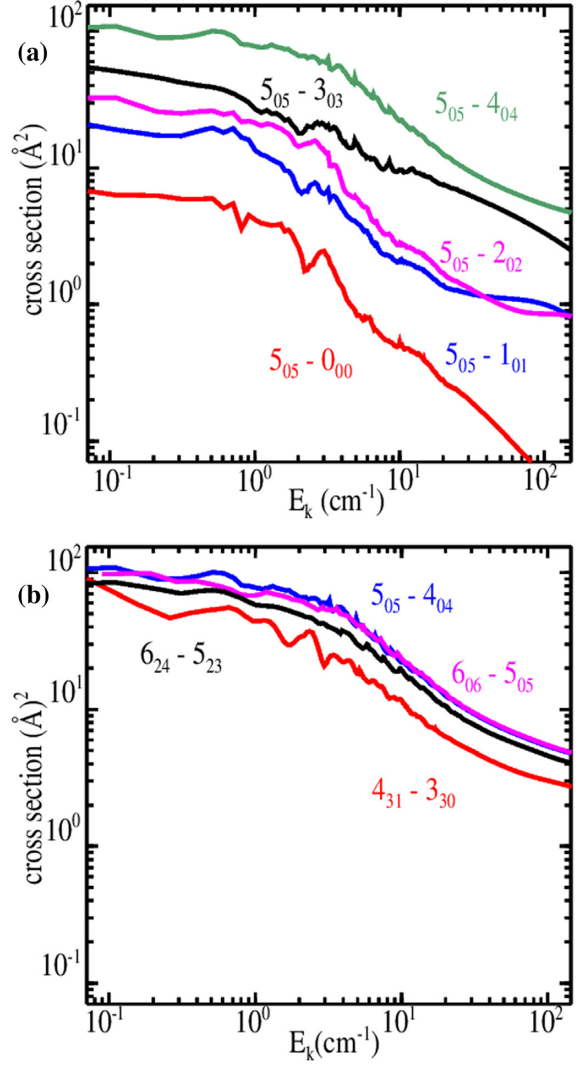

Figure 4. Evolution of the collision cross-sections as a function of kinetic energy E_k for some selected de-excitation transitions from the $5_{0,5}$ level (in a) and for some transitions where $\Delta K_a = 0$ and $\Delta K_c = \Delta j = -1$ (in b).

3.3 Rate coefficients

In order to obtain the thermal rate coefficients as a function of the kinetic temperature T, we need to integrate the calculated cross-sections over the Maxwell–Boltzmann distribution of kinetic energies as follows:

$$k_{jK_a,K_c \to j'K'_a,K'_c}(T) = \beta^2 \int_0^\infty E_k \sigma_{jK_a,K_c \to j'K'_a,K'_c}(E_k) e^{-\beta E_k} dE_k,$$

(4)

where $\beta = 1/k_B T$, with T, k_B, E_k, μ, and $\sigma_{jK_a, K_c \to j'K'_a, K'_c}$ are the kinetic temperature, the Boltzmann constant, the kinetic energy which is related to the total collisional energy according to $E = E_k + E_{jK_a, K_c}$, the reduced mass of the colliding system ($\mu = 3.7004$ au), and the cross-section from the initial rotational level j_{K_a, K_c} to the final rotational level $j'_{K'_a, K'_c}$.

The numerical integration in equation (4) was performed using the trapezoidal rule. The cross-sections computed for energies ranging from 1 to 170 cm^{-1}, lead to the calculation of rate coefficients for kinetic temperatures from $T = 1$–30 K and rotational levels up to $j_{K_aK_c} = 6_{3,3}$.
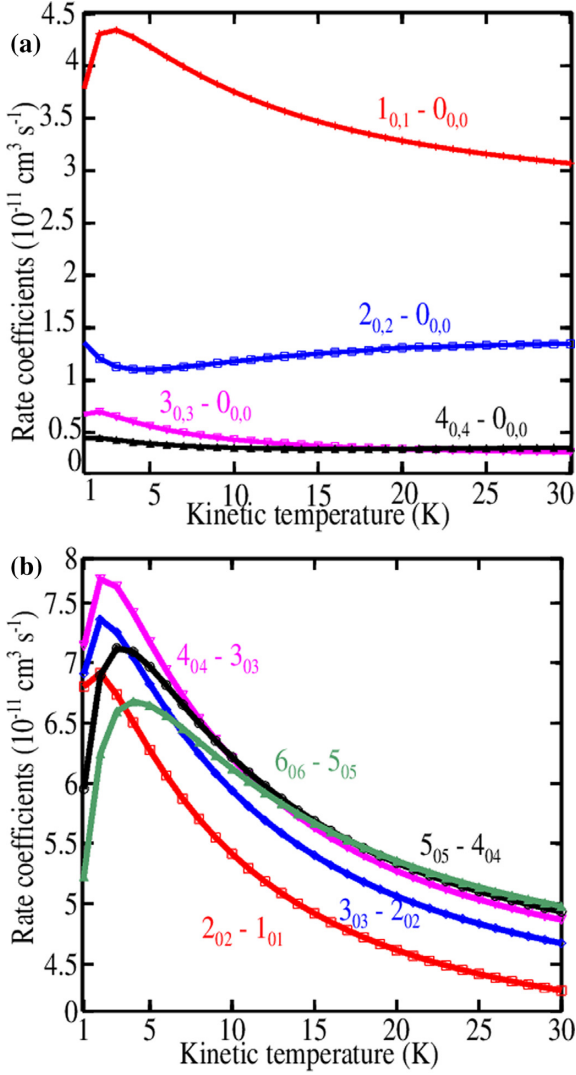
Figure 5. Variation of the rate coefficients versus kinetic temperature (T in K) for selected transitions corresponding to $j_{0,\,j}$–$0_{0,0}$ (a) and those with $\Delta j = -1$, $\Delta K_a = 0$, $\Delta j = \Delta K_c$ (b).

Figure 6. Variation of the downward rate coefficients for some $j_{0,\,j} \rightarrow j'_{0,\,j'}$ transitions with $\Delta j = -1, -2, -3$, $\Delta K_a = 0$, $\Delta K_c = \Delta j$ at $T = 10$ K.

Figure 7. Variation of the downward rate coefficients versus j for transitions with $\Delta j = -1$ and $\Delta K_c = \Delta j$ for $T = 5$, 10, and 25, in K.

Fig. 5 displays the rotational de-excitation rate coefficients of NaCN by collision with He atom as a function of kinetic temperature for different transitions. We give those from $j_{K_a K_c}$ state to the ground state $0_{0,0}$ ($\Delta j = -1, -2, -3, -4$ and $\Delta K_a = 0$, $\Delta K_c = \Delta j$) and those corresponding to $\Delta j = -1$, $\Delta K_a = 0$, and $\Delta K_c = \Delta j$ for $j = 1$–5. This figure shows that the rates exhibit smooth variations with the temperature for transitions associated with $\Delta j = -2, -3, -4$, and a decreasing shape when $\Delta j = -1$. As said above, the detected transitions $5_{0,5} \rightarrow 4_{0,4}$, $6_{0,6}$–$5_{0,5}$, and $4_{0,4} \rightarrow 3_{0,3}$ are dominant.

Fig. 6 displays the rate coefficients for some selected $j_{0,\,j} \rightarrow j'_{0,\,j'}$ transitions as a function of the rotational level j for $\Delta j = -1$, $-2, -3$, and for $T = 10$ K. As mentioned above $\Delta j = -1$ transitions are more favourable due to the dissymmetric shape of the NaCN–He potential. Fig. 7 shows the variation of the downward rate coefficients for transitions with $\Delta j = -1$ and $\Delta K_c = \Delta j$ as a function of j for selected temperatures ($T = 5$, 10, and 25, in K). These rate coefficients present the same behaviour. Indeed, they are a growing function of j values in the beginning for all selected temperatures and remain almost constant when j increases.
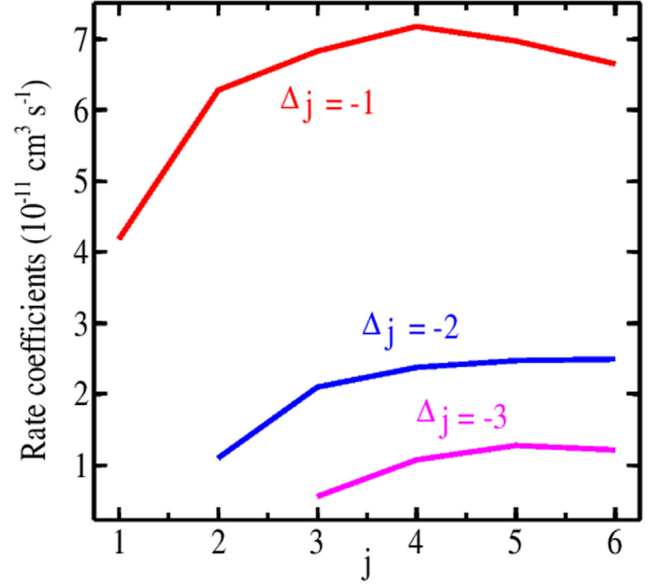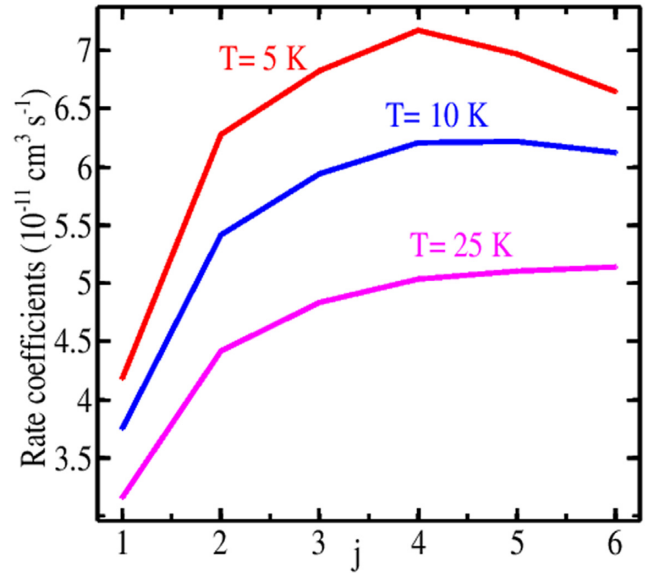
Mainly the NaCN–He rate coefficients decrease with increasing temperature following the behaviour observed for other colliding systems such as MgCN–He and AlCN–He (Hernandez et al. 2013). We also notice that the rate coefficients computed here for NaCN–He have the same order of magnitude ($\sim 10^{-11}$ cm^3 s^{-1}) as those deduced for MgCN–He and AlCN–He. This is because these metal cyanides possess close reduced masses and similar interaction potentials with He.

4 CONCLUSION

Quantum scattering calculations are done to determine the rotational de-excitation cross-sections and rate coefficients of sodium cyanide in collision with the He atom. Prior to that, we generated a 3D-PES

for the NaCN–He van der Waals complex at the CCSD(T)-F12/aug-cc-pVTZ level of theory. The analytical expansion of this 3D-PES was incorporated into dynamical calculations using the close coupling method (CC). The dynamical calculations were carried out for total energies ranging from 1 up to 170 cm^{-1}. Afterwards, the rate coefficients for the rotational (de-)excitation of the first 43 rotational levels of NaCN were determined for kinetic temperatures ranging from 1 to 30 K. Computations show the dominance of $\Delta j = \Delta K_c = -1$ transitions. This is related to the dissymmetric shape of the NaCN–He potential.

So far, NaCN is the most abundant detected metal cyanide in circumstellar gases (Pulliam et al. 2010), with abundances at least twice as high as those of other metal cyanides. Nevertheless, we compute rate coefficients of the NaCN–He colliding system of the same order of magnitude as those of other metal CN-containing molecules, such as MgCN–He and AlCN–He. This may be related to the different physical and chemical conditions under which these species are formed. For instance, NaCN is supposed to be an inner shell species (Guélin, Lucas & Cernicharo 1993; Highberger et al. 2001). AlNC is most likely present in the outer shell of IRC+10216 with a distribution extending deeper in the shell. Whereas the free radicals MgNC, its metastable isomer MgCN, and FeCN occupy shell-like distributions in the outer envelope (Guélin et al. 1993; Ziurys et al. 1995; Ziurys 2006; Zack et al. 2011), where photodissociation may largely contribute to their formation. These media are characterized by different temperatures ranging from 15 K to more than 100 K. Moreover, our data can be used for understanding and modelling the abundances and chemistry of NaCN in the astrophysical media as suggested recently by Quintana-Lacaci et al.(2017). Particularly, they should allow to go beyond the local thermodynamical equilibrium (LTE) conditions assumed by these authors for the modelling of the emission of NaCN. A more realistic derivation of the azimuthal averaged intensity profiles and thus of the abundance distribution of NaCN in these media should be obtained.

ACKNOWLEDGEMENTS

REFERENCES

Adler T. B., Knizia G., Werner H.-J., 2007, J. Chem. Phys. 127, 221106
Ajili Y., Hammami K., Jaidane N. E., Lanza M., Kalugina Y. N., Lique F., Hochlaf M., 2013, Phys. Chem. Chem. Phys., 15, 10062
Ajili Y., Trabelsi T., Denis-Alpizar O., Stoecklin T., Csaszar A. G., Mogren Al-Mogren M., Francisco J. S., Hochlaf M., 2016, Phys. Rev. A, 93, 052514
Al Mogren M. M., Denis-Alpizar O., Abdallah D. B., Stoecklin T., Halvick P., Senent M.-L., Hochlaf M., 2014, J. Chem. Phys., 141, 044308
Boys S. F., Bernardi F., 1970, Mol. Phys., 19, 553
Cernicharo J., Guelin M., 1987, A&A, 183, L10
Dunning T. H., 1989, J. Chem. Phys., 90, 1007
Garrison B. J., Lester W. A., Jr, Miller W. H., Jr, 1976, J. Chem. Phys., 65, 2193
Green S., 1976, J. Chem. Phys., 64, 3463
Green S., 1979, J. Chem. Phys., 67, 816
Guélin M., Lucas R., Cernicharo J., 1993, A&A, 280, L19
Guélin M., Muller S., Cernicharo J., Apponi A. J., McCarthy M. C., Gottlieb C. A., Thaddeus P., 2000, A&A, 363, L9
Guélin M., Muller S., Cernicharo J., McCarthy M. C., Thaddeus P., 2004, A&A, 426, L49
Halfen D. T., Ziurys L. M., 2011, ApJ, 730, 107
He J. H., Trung D.-V., Kwok S., Muller H. S. P., Zhang Y., Hasegawa T., Peng T. C., Huang Y. C., 2008, ApJS, 177, 275
Hernández Vera M., Lique F., Dumouchel F., Kłos J., Rubayo Soneira J., Senent M.-L., 2013, MNRAS, 432, 468
Highberger J. L., Savage C., Bieging J. H., Ziurys L. M., 2001, ApJ, 562, 790
Highberger J. L., Ziurys L. M., 2003, ApJ, 597, 1065
Hochlaf M., 2017, Phys. Chem. Chem. Phys., 19, 21236
Hutson J. M., Green S., 1994, MOLSCAT Computer Code, Version 14 (1994). Collaborative Computational Project No. 6 of the Engineering and Physical Sciences Research Council, UK
Kawaguchi K., Kagi E., Hirano T., Takano S., Saito S., 1993, ApJ, 406, L39
Kendall R. A., Dunning T. H., Harrison R. J., 1992, J. Chem. Phys., 96, 6796
Knizia G., Adler T. B., Werner H.-J., 2009, J. Chem. Phys., 130, 054104
Knowles P. J., Werner H.-J., 1985, Chem. Phys. Lett., 115, 259
Lara-Moreno M., Stoecklin T., Halvick P., Hochlaf M., 2019, Phys. Chem. Chem. Phys., 21, 3550
Lique F., Toboła R., Kłos J., Feautrier N., Spielfiedel A., Vincent L. F. M., Chałasiński G., Alexander M. H., 2008, A&A, 478, 567
Lique F., Kłos J., Hochlaf M., 2010, Phys. Chem. Chem. Phys., 12, 15672
Manolopoulos D. E., 1986, J. Chem. Phys., 85, 6425
McGuire B. A., 2018, ApJS, 239, 17
Müller H. S. P., Halfen D. T., Ziurys L. M., 2012, J. Mol. Spectrosc., 23, 272
Najar F., Ben Abdallah D., Jaidane N., Ben Lakhdar Z., Chambaud G., Hochlaf M., 2009, J. Chem. Phys., 130, 204305
Pulliam R. L., Savage C., Agúndez M., Cernicharo J., Guélin M., Ziurys L. M., 2010, ApJ, 725, L181
Quintana-Lacaci G., Cernicharo J., Velilla Prieto L., Agúndez M., Castro-Carrizo A., Fonfría J. P., Massalkhi S., Pardo J. R., 2017, A&A, 607, L5
Senent M. L., Dumouchel F., Lique F., 2012, MNRAS, 420, 1188
Tenenbaum E. D., Dodd J. L., Milan S. N., Woolf N. J., Ziurys L. M., 2010, ApJS, 190, 348
Turner B. E., Steimle T. C., Meerts L., 1994, ApJ, 426, L97
Werner H.-J., Knowles P. J., 1985, J. Chem. Phys. 82, 5053
Werner H.-J. et al., MOLPRO Version 2015 is a Package of ab initio Programs, http://www.molpro.net
Yousaf K. E., Peterson K. A., 2008, J. Chem. Phys., 129, 184108
Zack L. N., Halfen D. T., Ziurys L. M., 2011, ApJ, 733, L36
Ziurys L. M. 2006, PNAS, 103, 12274
Ziurys L. M., Apponi A. J., Guelin M., Cernicharo J., 1995, ApJ, 445, L47
Ziurys L. M., Savage C., Highberger J. L., Apponi A., Guélin J. M., Cernicharo J., 2002, Astrophys. J., 564, L45

SUPPORTING INFORMATION

Supplementary data are available at *MNRAS* online.
Figure S1 Comparison between analytical potentials and computed energies along the R Jacobi coordinate for $\theta = 0°$ and $\phi = 0°$ (left) and for $\theta = 180°$ and $\phi = 180°$ (right).
Table S1 Molecular properties of monomers NaCN and He calculated at MP2/aug-cc-pVQZ level of theory using finite-field method. All values are in au.

This paper has been typeset from a TeX/LaTeX file prepared by the author.

List of astronomical key words (Updated on 2017 March)

This list is common to *Monthly Notices of the Royal Astronomical Society, Astronomy and Astrophysics*, and *The Astrophysical Journal*. In order to ease the search, the key words are subdivided into broad categories. No more than *six* subcategories altogether should be listed for a paper.

The subcategories in boldface containing the word 'individual' are intended for use with specific astronomical objects; these should never be used alone, but always in combination with the most common names for the astronomical objects in question. Note that each object counts as one subcategory within the allowed limit of six.

The parts of the key words in italics are for reference only and should be omitted when the keywords are entered on the manuscript.

General
editorials, notices
errata, addenda
extraterrestrial intelligence
history and philosophy of astronomy
miscellaneous
obituaries, biographies
publications, bibliography
sociology of astronomy
standards

Physical data and processes
acceleration of particles
accretion, accretion discs
asteroseismology
astrobiology
astrochemistry
astroparticle physics
atomic data
atomic processes
black hole physics
chaos
conduction
convection
dense matter
diffusion
dynamo
elementary particles
equation of state
gravitation
gravitational lensing: micro
gravitational lensing: strong
gravitational lensing: weak
gravitational waves
hydrodynamics
instabilities
line: formation
line: identification
line: profiles
magnetic fields
magnetic reconnection
(magnetohydrodynamics) MHD
masers
molecular data
molecular processes
neutrinos
nuclear reactions, nucleosynthesis, abundances
opacity
plasmas
polarization

radiation: dynamics
radiation mechanisms:general
radiation mechanisms: non-thermal
radiation mechanisms: thermal
radiative transfer
relativistic processes
scattering
shock waves
solid state: refractory
solid state: volatile
turbulence
waves

Astronomical instrumentation, methods and techniques
atmospheric effects
balloons
instrumentation: adaptive optics
instrumentation: detectors
instrumentation: high angular resolution
instrumentation: interferometers
instrumentation: miscellaneous
instrumentation: photometers
instrumentation: polarimeters
instrumentation: spectrographs
light pollution
methods: analytical
methods: data analysis
methods: laboratory: atomic
methods: laboratory: molecular
methods: laboratory: solid state
methods: miscellaneous
methods: numerical
methods: observational
methods: statistical
site testing
space vehicles
space vehicles: instruments
techniques: high angular resolution
techniques: image processing
techniques: imaging spectroscopy
techniques: interferometric
techniques: miscellaneous
techniques: photometric
techniques: polarimetric
techniques: radar astronomy
techniques: radial velocities
techniques: spectroscopic
telescopes

Astronomical data bases
astronomical data bases: miscellaneous
atlases
catalogues
surveys
virtual observatory tools

Astrometry and celestial mechanics
astrometry
celestial mechanics
eclipses
ephemerides
occultations
parallaxes
proper motions
reference systems
time

The Sun
Sun: abundances
Sun: activity
Sun: atmosphere
Sun: chromosphere
Sun: corona
Sun: coronal mass ejections (CMEs)
Sun: evolution
Sun: faculae, plages
Sun: filaments, prominences
Sun: flares
Sun: fundamental parameters
Sun: general
Sun: granulation
Sun: helioseismology
Sun: heliosphere
Sun: infrared
Sun: interior
Sun: magnetic fields
Sun: oscillations
Sun: particle emission
Sun: photosphere
Sun: radio radiation
Sun: rotation
(Sun:) solar–terrestrial relations
(Sun:) solar wind
(Sun:) sunspots
Sun: transition region
Sun: UV radiation
Sun: X-rays, gamma-rays

Planetary systems
comets: general

comets: individual: . . .
Earth
interplanetary medium
Kuiper belt: general

Kuiper belt objects: individual: . . .
meteorites, meteors, meteoroids
minor planets, asteroids: general

minor planets, asteroids: individual: . . .

Moon
Oort Cloud
planets and satellites: atmospheres
planets and satellites: aurorae
planets and satellites: composition
planets and satellites: detection
planets and satellites: dynamical evolution and stability
planets and satellites: formation
planets and satellites: fundamental parameters
planets and satellites: gaseous planets
planets and satellites: general

planets and satellites: individual: . . .
planets and satellites: interiors
planets and satellites: magnetic fields
planets and satellites: oceans
planets and satellites: physical evolution
planets and satellites: rings
planets and satellites: surfaces
planets and satellites: tectonics
planets and satellites: terrestrial planets
planet–disc interactions
planet–star interactions
protoplanetary discs
zodiacal dust

Stars
stars: abundances
stars: activity
stars: AGB and post-AGB
stars: atmospheres
(stars:) binaries *(including multiple)*: close
(stars:) binaries: eclipsing
(stars:) binaries: general
(stars:) binaries: spectroscopic
(stars:) binaries: symbiotic
(stars:) binaries: visual
stars: black holes
(stars:) blue stragglers
(stars:) brown dwarfs
stars: carbon
stars: chemically peculiar
stars: chromospheres
(stars:) circumstellar matter
stars: coronae
stars: distances
stars: dwarf novae
stars: early-type
stars: emission-line, Be
stars: evolution
stars: flare
stars: formation
stars: fundamental parameters
(stars:) gamma-ray burst: general
(stars:) **gamma-ray burst: individual: . . .**
stars: general
(stars:) Hertzsprung–Russell and colour–magnitude diagrams
stars: horizontal branch
stars: imaging
stars: individual: . . .
stars: interiors

stars: jets
stars: kinematics and dynamics
stars: late-type
stars: low-mass
stars: luminosity function, mass function
stars: magnetars
stars: magnetic field
stars: massive
stars: mass-loss
stars: neutron
(stars:) novae, cataclysmic variables
stars: oscillations *(including pulsations)*
stars: peculiar *(except chemically peculiar)*
(stars:) planetary systems
stars: Population II
stars: Population III
stars: pre-main-sequence
stars: protostars
(stars:) pulsars: general
(stars:) **pulsars: individual: . . .**
stars: rotation
stars: solar-type
(stars:) starspots
stars: statistics
(stars:) subdwarfs
(stars:) supergiants
(stars:) supernovae: general
(stars:) **supernovae: individual: . . .**
stars: variables: Cepheids
stars: variables: Scuti
stars: variables: general
stars: variables: RR Lyrae
stars: variables: S Doradus
stars: variables: T Tauri, Herbig Ae/Be
(stars:) white dwarfs
stars: winds, outflows
stars: Wolf–Rayet

Interstellar medium (ISM), nebulae
ISM: abundances
ISM: atoms
ISM: bubbles
ISM: clouds
(ISM:) cosmic rays
(ISM:) dust, extinction
ISM: evolution
ISM: general
(ISM:) HII regions
(ISM:) Herbig–Haro objects

ISM: individual objects: . . .
(except planetary nebulae)
ISM: jets and outflows
ISM: kinematics and dynamics
ISM: lines and bands
ISM: magnetic fields
ISM: molecules
(ISM:) photodissociation region (PDR)
(ISM:) planetary nebulae: general
(ISM:) **planetary nebulae: individual: . . .**
ISM: structure
ISM: supernova remnants

The Galaxy
Galaxy: abundances
Galaxy: bulge
Galaxy: centre
Galaxy: disc
Galaxy: evolution
Galaxy: formation
Galaxy: fundamental parameters
Galaxy: general
(Galaxy:) globular clusters: general
(Galaxy:) **globular clusters: individual: . . .**
Galaxy: halo
Galaxy: kinematics and dynamics
(Galaxy:) local interstellar matter
Galaxy: nucleus
(Galaxy:) open clusters and associations: general
(Galaxy:) **open clusters and associations: individual: . . .**
(Galaxy:) solar neighbourhood
Galaxy: stellar content
Galaxy: structure

Galaxies
galaxies: abundances
galaxies: active
(galaxies:) BL Lacertae objects: general
(galaxies:) **BL Lacertae objects: individual: . . .**
galaxies: bulges
galaxies: clusters: general

galaxies: clusters: individual: . . .
galaxies: clusters: intracluster medium
galaxies: distances and redshifts
galaxies: dwarf
galaxies: elliptical and lenticular, cD
galaxies: evolution
galaxies: formation
galaxies: fundamental parameters
galaxies: general
galaxies: groups: general

galaxies: groups: individual: . . .
galaxies: haloes
galaxies: high-redshift

galaxies: individual: . . .
galaxies: interactions
(galaxies:) intergalactic medium
galaxies: irregular
galaxies: ISM
galaxies: jets
galaxies: kinematics and dynamics
(galaxies:) Local Group
galaxies: luminosity function, mass function
(galaxies:) Magellanic Clouds
galaxies: magnetic fields
galaxies: nuclei
galaxies: peculiar
galaxies: photometry
(galaxies:) quasars: absorption lines
(galaxies:) quasars: emission lines
(galaxies:) quasars: general

(galaxies:) **quasars: individual: . . .**
(galaxies:) quasars: supermassive black holes
galaxies: Seyfert
galaxies: spiral
galaxies: starburst
galaxies: star clusters: general

galaxies: star clusters: individual: . . .
galaxies: star formation
galaxies: statistics
galaxies: stellar content
galaxies: structure

Cosmology
(cosmology:) cosmic background radiation
(cosmology:) cosmological parameters
(cosmology:) dark ages, reionization, first stars
(cosmology:) dark energy
(cosmology:) dark matter
(cosmology:) diffuse radiation
(cosmology:) distance scale
(cosmology:) early Universe
(cosmology:) inflation
(cosmology:) large-scale structure of Universe
cosmology: miscellaneous
cosmology: observations
(cosmology:) primordial nucleosynthesis
cosmology: theory

Resolved and unresolved sources as a function of wavelength
gamma-rays: diffuse background
gamma-rays: galaxies
gamma-rays: galaxies: clusters
gamma-rays: general
gamma-rays: ISM
gamma-rays: stars
infrared: diffuse background
infrared: galaxies
infrared: general
infrared: ISM
infrared: planetary systems
infrared: stars
radio continuum: galaxies
radio continuum: general
radio continuum: ISM
radio continuum: planetary systems
radio continuum: stars
radio continuum: transients
radio lines: galaxies
radio lines: general
radio lines: ISM
radio lines: planetary systems
radio lines: stars
submillimetre: diffuse background
submillimetre: galaxies
submillimetre: general
submillimetre: ISM
submillimetre: planetary systems
submillimetre: stars
ultraviolet: galaxies

ultraviolet: general
ultraviolet: ISM
ultraviolet: planetary systems
ultraviolet: stars
X-rays: binaries
X-rays: bursts
X-rays: diffuse background
X-rays: galaxies
X-rays: galaxies: clusters
X-rays: general
X-rays: individual: . . .
X-rays: ISM
X-rays: stars